

# Lensed quasars in CatNorth I. Wide-separation candidates

Di Wu<sup>1,2</sup>, Zizhao He<sup>4,★</sup>, Nan Li<sup>1,2,3,★★</sup>, Shenzhe Cui<sup>1,2</sup>, Yuming Fu<sup>7,8</sup>, Xue-Bing Wu<sup>5,6</sup>, and Dan Qiu<sup>5</sup>

<sup>1</sup> National Astronomical Observatories, Chinese Academy of Sciences, 20A Datun Road, Chaoyang District, Beijing 100101, China  
e-mail: nan.li@nao.cas.cn

<sup>2</sup> School of Astronomy and Space Science, University of Chinese Academy of Sciences, Beijing 100049, China

<sup>3</sup> Key Laboratory of Space Astronomy and Technology, National Astronomical Observatories, Chinese Academy of Sciences, 20A Datun Road, Chaoyang District, Beijing 100101, China

<sup>4</sup> Purple Mountain Observatory, Chinese Academy of Sciences, Nanjing, Jiangsu, 210023, China  
e-mail: zzhe@pmo.ac.cn

<sup>5</sup> Kavli Institute for Astronomy and Astrophysics, Peking University, Yi He Yuan Lu 5, Haidian Qu, 100871 Beijing, People's Republic of China

<sup>6</sup> Department of Astronomy, School of Physics, Peking University, Beijing 100871, Peoples Republic of China

<sup>7</sup> Leiden Observatory, Leiden University, P.O. Box 9513, NL-2300 RA Leiden, The Netherlands

<sup>8</sup> Kapteyn Astronomical Institute, University of Groningen, P.O. Box 800, NL-9700 AV Groningen, The Netherlands

## ABSTRACT

**Context.** Wide-separation lensed quasars (WSLQs) represent a special but rare subclass of strongly lensed quasars with multiple images, magnified by massive galaxy cluster lenses, which offer valuable probes for the properties of dark matter halos and detailed characteristics of quasar host galaxies. However, only  $\sim 10$  WSLQ systems limit the development of relevant investigations.

**Aims.** To enlarge the sample of WSLQs by mining candidates from large-scale sky surveys, we develop a catalog-based pipeline and apply it to the CatNorth database, which is a quasar candidates catalog constructed from *Gaia* DR3, comprises 1,545,514 quasar candidates, achieves a purity of  $\sim 90\%$  and has a limiting magnitude of *Gaia* G band  $\lesssim 21$ .

**Methods.** The pipeline unfolds in three sequential stages. First, to search for groups of quasar candidates with a maximum quasar image separation exceeding 10 arcsec but less than  $\sim 72$  arcsec, we apply a Friends-of-Friends-like algorithm, based on HEALPix with a grid size of 25.6 arcsec, to the projected sky coordinates of the objects in CatNorth. Second, these identified groups undergo an automated filtering process that assesses the intra-group similarity of photometric colours or spectral information when available. These two steps reduce the original CatNorth dataset from 1,545,514 quasar candidates to a sample of 14,244 quasar candidate groups, while retaining all discoverable previously known WSLQs. Third, a visual inspection, guided primarily by the projected geometry of the quasar images and plausible foreground objects, yields the final candidate sample with a label indicating their quality.

**Results.** We have identified a total of 333 new WSLQ candidates with separations ranging from 10 to 56.8 arcsec. By exploiting the available SDSS DR16/DESI DR1 spectroscopic data, we uncover two novel WSLQ candidate systems, but 331 WSLQ candidates lack sufficient spectral information, comprising 45 Grade-A, 98 Grade-B, and 188 Grade-C systems. In addition, a sample of 29 confirmed dual quasars is presented as a by-product. When feasible, we plan to secure follow-up spectroscopy and deeper imaging to confirm WSLQs from the above candidates and proceed with pertinent scientific investigations.

**Key words.** gravitational lensing: strong – Galaxies: quasars: general – Galaxies: clusters: general – methods: data analysis – Catalogs

## 1. Introduction

Strongly lensed quasars arise when the foreground dark-matter halo lies nearly along the line of sight to a background quasar and the halo's gravitational potential then splits the quasar's light into multiple images through the lensing effect (Walsh et al. 1979). Such multiply imaged strongly lensed quasar systems are of high scientific value, which can be used to study the properties of active galactic nuclei (AGN) through microlensing effects caused by stars in the foreground galaxies (Anguita et al. 2008; Motta et al. 2012; Fian et al. 2024) and measure the Hubble constant via time-delay measurements and to explore the properties of dark matter (Oguri et al. 2014; Suyu et al. 2014; Wong et al. 2020; Kochanek 2020; Sonnenfeld 2021).

In particular, as a species of lensed quasar, the wide-separation lensed quasar (WSLQ) whose maximum separation

is greater than 10 arcsec (Napier et al. 2023) holds particular scientific value. These systems are produced by galaxy group or galaxy cluster scale dark matter halos' gravitational lensing effect, and their wide separations allow observations of the quasar along multiple, wide-separated lines of sight, which facilitates constructing the three-dimensional spatial distribution of outflows (Misawa et al. 2013, 2014; Misawa et al. 2016). The image positions, time delays, and magnification factors of WSLQs can place constraints on the mass distributions of the cluster-scale dark matter halos (Sharon et al. 2017; Martinez et al. 2023; Napier et al. 2023). Moreover, the wide separations and high magnifications of WSLQs help resolve quasar host galaxies (Bayliss et al. 2017; Cloonan et al. 2024).

The number of WSLQs remains limited. To date, approximately 300 lensed quasars have been discovered (see, e.g. Lemon et al. 2022), among them 8 are WSLQs (Inada et al. 2003, 2006; Oguri et al. 2008; Dahle et al. 2013; Shu et al. 2018, 2019; Stern et al. 2021; Martinez et al. 2023; Napier et al. 2023).

\* zzhe@pmo.ac.cn

\*\* nan.li@nao.cas.cn

Despite these findings, significant potential remains for further discoveries of WSLQs within currently available datasets, because the observed number remains far below the prediction. [Robertson et al. \(2020\)](#) pointed out that for a point source being highly magnified (magnification factor  $> 10$ ) at  $z = 2$  which is the typical redshift of quasar ([Pâris et al. 2018](#); [Collaboration et al. 2025](#)), the probability that a lensed quasar was lensed by a halo with  $M_{200} > 10^{14} \text{ M}_\odot$  and  $> 10^{13} \text{ M}_\odot$  are around 25% and 50% respectively.

In the process of searching for lensed quasars, dual quasars can often be found as a by-product ([He et al. 2025](#)). Dual quasars refer to physically associated quasar pairs, typically separated by 1 pc to 100 kpc ([De Rosa et al. 2019](#)), the corresponding angular separation extends to the size of  $\sim 12$  arcsec at redshift 2 in the  $\Lambda\text{CDM}$  universe. They are often a by-product of the search for lensed quasars because the member quasars of dual quasars lie close to one another in angular position on the sky, which is similar to the angular position relation between the member images of multiply lensed quasar images. Dual quasars serve as valuable objects for investigating the galaxy merger process and the properties of supermassive black holes ([Boylan-Kolchin et al. 2008](#); [Roedig et al. 2014](#); [Romero et al. 2016](#); [Martin et al. 2018](#)). Nevertheless, the number of dual quasars is limited to about  $\sim 500$  cases (see e.g. [Hennawi et al. 2010](#)).

In this work, we generate a WSLQ candidate catalogue based on the quasar group finding algorithm adopted from [He et al. \(2023\)](#) and a new high-quality quasar candidates catalogue CatNorth ([Fu et al. 2024](#)) which is generated based on the Gaia DR3 quasar candidates catalogue. Besides, we generate a dual quasar catalogue. The purity of the CatNorth quasar candidates catalogue is up to 90%, while the primordial GDR3 quasar candidate catalogue only has a purity of about 52% ([Gaia Collaboration et al. 2023b](#)). The higher purity helps reduce the false positive rate of lensed quasar searching. The selection has three stages. First, we group CatNorth quasar candidates on the sky with a HEALPix-based Friends-of-Friends-like algorithm, clustering objects that are adjacent in projection. Second, we keep only groups whose maximum pairwise separation exceeds 10 arcsec and subject them to an automated filter that assesses intra-group similarity in photometric colours or, when available, spectroscopic consistency by the spectrum retrieved from several spectrum datasets. Together these steps reduce CatNorth from 1 545 514 candidates to 14 244 quasar candidate groups. Finally, visual inspection guided by the image geometry and the presence of plausible foreground deflectors yields the final candidate sample with an assigned quality label. For the final candidate sample, we perform the cross match with three catalogues of a total of about 1.9 million galaxy clusters to find the highly probable WSLQ candidates. Besides, we estimated the completeness of our WSLQ candidates catalogue by testing the discoverable rate of the known WSLQs and assessing our searching algorithm by examining the recovery rate of discoverable WSLQs.

The paper is organised as follows. Section 2 introduces the datasets we utilised in this work. In Section 3, we detail our quasar group finding algorithm and the further screening method. The results of the WSLQ candidates catalogue and quasar dual candidates catalogue are shown in Section 4. And the Section 5 and 6 include the discussion and the conclusion of this work, respectively. We adopt a  $\Lambda\text{CDM}$  cosmology in which parameters are from Planck 2018 results ([Planck Collaboration et al. 2020](#)). Unless otherwise stated, all magnitudes quoted in this paper are in the AB system.

## 2. Datasets

Our analysis is anchored in CatNorth, its properties are summarised in Section 2.1. To aid in the selection of high-value lensed quasar candidates and assess the reliability of our algorithm, we further draw on several auxiliary resources, including spectroscopic archives, galaxy cluster catalogues, and discoverable known WSLQs in CatNorth, introduced in Sections 2.2, 2.3, and 2.4 respectively.

### 2.1. CatNorth

Our search for lensed quasar candidates is performed based on the CatNorth ([Fu et al. 2024](#)). CatNorth lists 1 545 514 quasar candidates extracted from the approximately 6.6 million sources in the *Gaia* DR3 quasar candidate catalogue ([Gaia Collaboration et al. 2023a](#)) and raises the purity to about 90 per cent by a machine learning pipeline trained on the proper motions, parallaxes and multi-band colours information of robust celestial object samples. During this process ([Fu et al. 2024](#)) utilised  $g$ ,  $r$ ,  $i$ ,  $z$  and  $y$  photometry from Pan-STARRS1 ([Chambers et al. 2016](#)) together with  $W1$  and  $W2$  photometry from the CatWISE2020 ([Marocco et al. 2021](#)) and incorporated these information in the final CatNorth table. CatNorth covers about  $3\pi$  steradians of sky and has a limiting magnitude of  $\lesssim 21$  in the *Gaia*  $G$  band. For each quasar candidate, it also provides a photometric redshift  $z_{\text{ph}}$ , derived using an ensemble regression model. Owing to its large area and high purity, CatNorth constitutes a suitable parent sample for the discovery of WSLQs and dual quasars.

### 2.2. Spectrum dataset

To refine the lensed quasar candidate and dual quasar samples, we retrieve the relevant optical spectra from two spectroscopic surveys: SDSS Data Release 16 (SDSS DR16; [Ahumada et al. 2020](#)) and the DESI Data Release 1 (DESI DR1; [Collaboration et al. 2025](#)).

The Sloan Digital Sky Survey (SDSS) is conducted at the Apache Point Observatory (APO) ([York et al. 2000](#); [Eisenstein et al. 2011](#); [Blanton et al. 2017](#)). The quasar catalogue of the SDSS sixteenth data release (DR16) ([Lyke et al. 2020](#)) compiles all quasar spectra obtained since the inception of SDSS ([Richards et al. 2002](#); [Dawson et al. 2013](#); [Dawson et al. 2016](#)), including observations from the Baryon Oscillation Spectroscopic Survey (BOSS) ([Dawson et al. 2013](#)) and the Extended BOSS (eBOSS) ([Dawson et al. 2016](#)), and contains a total of 750 414 quasars, of which  $\sim 500\,000$  lie in the redshift range  $0.8 < z < 2.2$  ([Dawson et al. 2016](#)).

The Dark Energy Spectroscopic Instrument (DESI) is carried out by the Mayall 4 m Telescope at Kitt Peak National Observatory (KPNO) ([Levi et al. 2013](#); [Collaboration et al. 2016, 2022](#)). The first public data release, DESI DR1 ([Collaboration et al. 2025](#)), constitutes a milestone for spectroscopic sky surveys, providing spectra for 1 647 484 quasars reaching a maximum redshift of  $z = 6.86$ ; about 95% of these quasars lie at redshifts  $z \sim 0\text{--}3$ .

For objects with existing spectra in these catalogues, we apply an automated filter to reject quasar groups in which line-of-sight velocities of group members are obviously different, while flagging a subset of high-priority lensed quasar candidates. In addition to lensed quasar candidates, we also yield a catalogue of confirmed dual quasars based on quasar groups' projected separation and line-of-sight velocity difference. Details of the filtering are given in Section 3.2.

### 2.3. Galaxy cluster catalogue

We cross match WSLQ candidates obtained in this work with several galaxy group and galaxy cluster catalogues. Systems whose image separations exceed 10 arcsec at a typical redshift configuration (lens redshift at 0.5 and source redshift at 2) require a massive deflector of  $\sigma_v \gtrsim 740 \text{ km s}^{-1}$  under the simple SIS assumption, typically a galaxy group or cluster (Sharon et al. 2020); thus the presence of a known cluster near a candidate improve the probability that the system is a real WSLQ.

We employ three galaxy cluster catalogues: the compilation of Wen & Han (2024) (hereafter WEN\_CAT), the catalogue from Zou et al. (2021) (hereafter ZOU\_CAT), and the eRASS1 Galaxy groups and clusters primary catalogue (Bulbul et al. 2024) (hereafter ERO\_CAT). The WEN\_CAT and ZOU\_CAT catalogues comprise close to two million galaxy clusters, offering a particularly rich resource for our studies. The ERO\_CAT, constructed from X-ray observations, is a galaxy cluster/group catalogue that can serve as a valuable complement to these datasets. In particular, WEN\_CAT lists 1 581 179 clusters with  $M_{500} > 4.7 \times 10^{13} M_\odot$ , the median mass is  $7.9 \times 10^{13} M_\odot$  and redshifts reach  $z \approx 1.5$ . ZOU\_CAT contains 540 432 clusters with a median  $M_{500} = 1.23 \times 10^{14} M_\odot$  and  $z \leq 1$ . ERO\_CAT comprises 12 247 clusters and groups spanning  $5 \times 10^{12} M_\odot < M_{500} < 2 \times 10^{15} M_\odot$  and extending to  $z = 1.32$ . Roughly 40 per cent of ZOU\_CAT objects and ninety per cent of ERO\_CAT objects have counterparts in WEN\_CAT. These catalogues allow us to mark the lensed quasar candidates that lie near known clusters and to single out high-priority systems. The relevant cross matching process is presented in Section 4.1.

### 2.4. Discoverable known lenses

Up to now, 8 WSLQ systems are known; by the fraction of these lenses that appear in the CatNorth and the fraction of discoverable known lenses that successfully pass through our pipeline, we can estimate the completeness of CatNorth and evaluate the reliability of our lensed quasar candidates search algorithm.

Among the eight known WSLQs, four are present in CatNorth: J1004+4112 (Inada et al. 2003), SDSS J1029+2623 (Inada et al. 2006; Oguri et al. 2008), SDSS J1326+4806 (Shu et al. 2019), and GrAL J165105.3-041725 (Stern et al. 2021); the remaining WSLQs are missing because they fall below the CatNorth's limiting magnitude, with only the brightest image of COOL J0542-2125 (Martinez et al. 2023) in the DESI Legacy Imaging Surveys DR9 having a counterpart image in CatNorth. This yields a coverage of approximately 50% for the known WSLQs within CatNorth. For the four discoverable lenses, CatNorth contains only two images each, their image cutouts are displayed from left to right in Figure 1, while the intrinsic image multiplicities of these systems are 4, 3, 2, and 4 from left to right, respectively. In Section 5.1, we assess the performance of these known lenses in our search pipeline and, on that basis, infer the reliability of our algorithm.

## 3. Methodology

Search for WSLQ and dual quasars in CatNorth is carried out in three stages, summarised in Figure 2. First, we apply the group finder in He et al. (2023) to the projected sky positions of quasar candidates in CatNorth to form a quasar group samples and retain only those quasar groups whose maximum pairwise separation is greater than 10 arcsec, which is the typical scale of galaxy cluster lensed quasar, full details are given in Section 3.1.

Groups in CatNorth with maximum image separation smaller than 10 arcsec are analysed in a companion work (He et al., in prep.). Second, an automated filter based on the spectroscopic and photometric similarity of the members within each group is performed, as described in Section 3.2. All discoverable known WSLQs present in CatNorth survive these two steps. Third, a visual inspection based on the projected spatial configuration of the group members and the plausible foreground object yields the final samples of lensed quasar candidates and dual quasars, outlined in Section 3.3.

### 3.1. Quasar group finder

We adopt the quasar group search algorithm from He et al. (2023) to construct a catalogue of quasar candidate groups whose members' projected angular positions are adjacent on the sky. All CatNorth sources are first assigned to the grid defined by Hierarchical Equal Area isoLatitude Pixelization (HEALPix; Gorski et al. 1999) with  $N_{\text{side}} = 2^{13}$ ; this choice gives an angular resolution of about 25.6 arcsec and a total of  $0.81 \times 10^9$  grids. The 1 545 514 objects in CatNorth occupy 1 542 794 distinct grids. Grids containing at least two candidates while none of their eight neighbours host any candidates form the Case 1 of the quasar candidates group samples, which comprises 2 636 groups. Then, starting from every grid that contains at least one quasar candidate, we examine its surrounding grids; whenever additional candidates are found, they are iteratively collected, together with their neighbouring grids, until no further quasar candidates appear. Each assembly of candidates obtained in this way, together with those in the initial pixel, defines a sample labelled Case 2; it contains 20 096 groups. Combining Case 1 and Case 2 yields 22 732 quasar candidate groups, which we refer to as the quasar group catalogue (QGC).

Within the QGC, 22 280 groups contain exactly two quasar candidates, whereas 452 groups contain three or more. To improve the efficiency of later filters, each of the latter groups (which contains three or more members) is decomposed as follows. For a group with  $N$  members, every internal combination containing between two and  $N - 1$  members is treated as a separate group and appended to the QGC. This step adds 1 669 new groups, raising the catalogue size to 24 401. The decomposition prevents real lens systems from being rejected during the colour similarity filtering described in Section 3.2, when they primordially reside in otherwise groups contaminated by some chance adjacent quasar candidates which have quite different colours.

### 3.2. Automated screening

From the roughly 24 000 quasar groups returned by the group finder, we conducted a series of automated screenings. We first exclude systems whose maximum pairwise separation does not exceed 10 arcsec. Then, because the optical spectra and colours of multiple images in a lensed quasar are expected to be highly alike (Appendix A outlines the physical mechanisms that can introduce minor deviations in optical spectra), we then apply an automated filter based on spectroscopic or photometric similarity to eliminate groups whose members display pronounced discrepancies.

For the aim of automated screening based on the available spectroscopic data, we cross match the positions of member quasar candidates in each group with the SDSS DR16 and DESI DR1 within a 1 arcsec radius. We found 6 730 groups pos-

**Table 1.** Eight known wide-separation lensed quasars (WSLQs) and their basic properties. “sep<sub>max</sub>” is the largest image separation within the system. “N” is the intrinsic image multiplicity. “CatNorth imgs” is the number of counterpart images found in CatNorth. “Discoverable” denotes whether the system is discoverable within CatNorth (i.e. has  $\geq 2$  counterpart images); \* denotes photometric redshift. The column Brightest Image refers to the g magnitude of the brightest image within the systems; the data is from DESI DR9, except that the \*\* denotes the g magnitude data from Pan-STARRS1.

No.	System	$z_s$	$z_l$	sep <sub>max</sub> (arcsec)	N	CatNorth imgs	Discoverable	Brightest Image (mag)	Notes / Refs
1	SDSS J1004+4112	1.734	0.68	14.62	4	2	Yes	19.73	Inada et al. (2003)
2	SDSS J1029+2623	2.197	0.596	22.5	3	2	Yes	18.85	Inada et al. (2006); Oguri et al. (2008)
3	SDSS J1326+4806	2.08	0.396	21.06	2	2	Yes	20.23	Shu et al. (2019)
4	GraL J165105.3–041725	1.451	0.591	10.1	4	2	Yes	19.6**	Stern et al. (2021)
5	SDSS J2222+2745	2.805	0.49	15.1	6	0	No	20.65	Dahle et al. (2013)
6	SDSS J0909+4449	2.788	0.9*	13.86	3	0	No	21.58	Shu et al. (2018)
7	COOL J0542–2125	1.84	0.61	25.9	3	1	No	20.68	Only brightest image in DESI DR9 matched; Martinez et al. (2023)
8	COOL J0335–1927	3.27	0.4178	23.3	3	0	No	21.37	Napier et al. (2023)

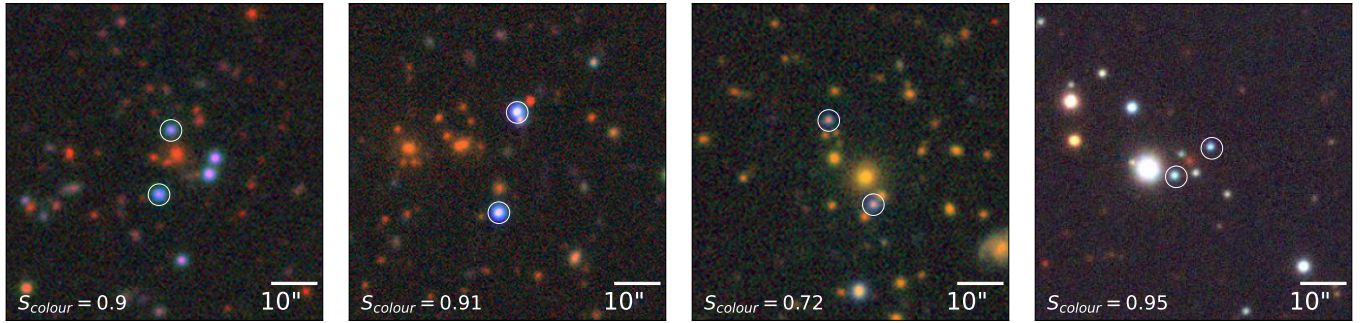


**Fig. 1.** Optical images of the four discoverable wide-separation lensed quasars. From left to right: SDSS J1004+4112, SDSS J1029+2623, SDSS J1326+4806, and GraL J165105.3–041725. Quasar images included in CatNorth are marked with white circles. The images of the first three panels are from DESI Legacy Imaging Surveys DR9, and the rightmost panel is from Pan-STARRS1. (Orientation: west is left and east is right; same hereafter.)

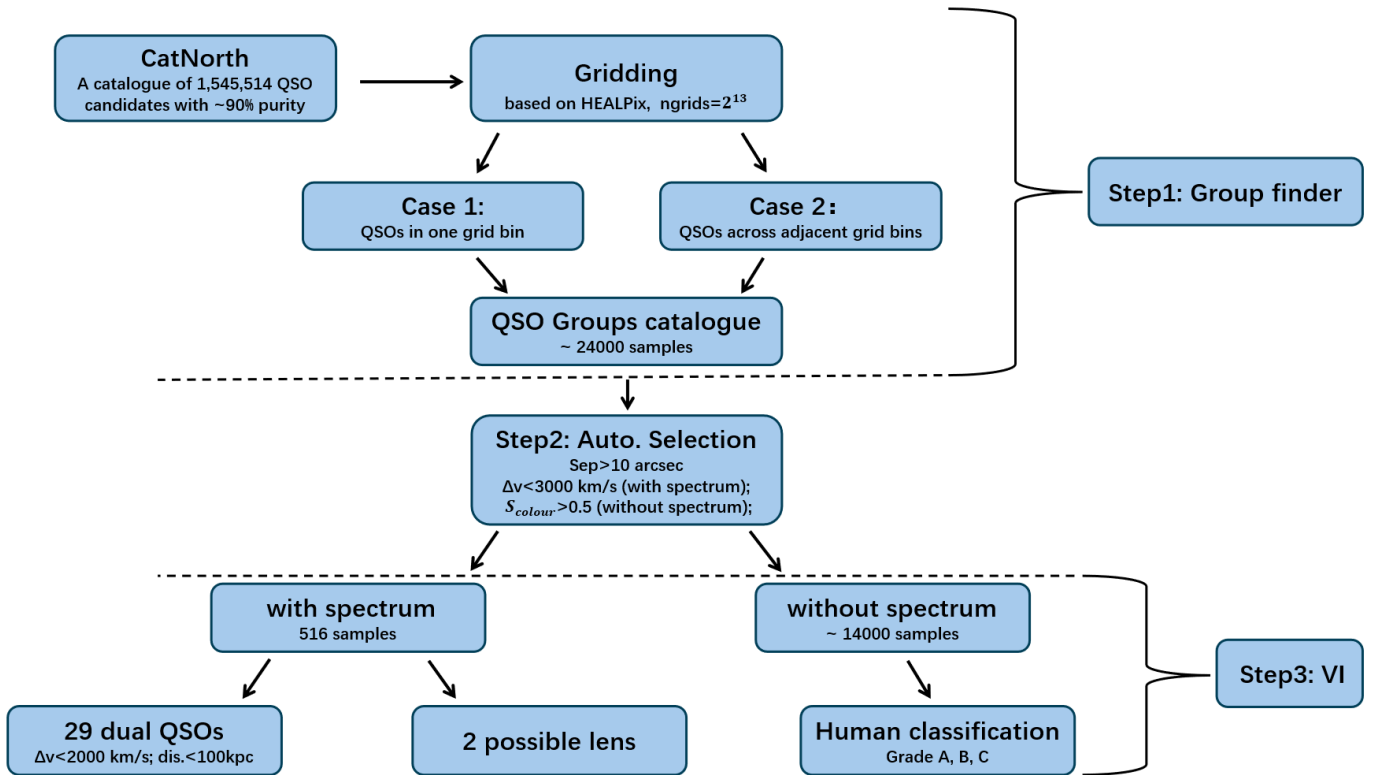


**Fig. 2.** Flowchart illustrating the methodology employed to select wide-separation lensed quasar candidates and dual quasars from the CatNorth.

sess spectra for at least two members<sup>1</sup>. For every pair of spectra of member quasar candidates in such a group, we compute the velocity difference by (Hogg 2000):

$$\Delta v = c \frac{\Delta z}{1 + z_{\text{mean}}}, \quad (1)$$

where  $\Delta z$  is the redshift difference,  $z_{\text{mean}}$  is the average redshift of the pair, and  $c$  is the speed of light in vacuum. Groups containing any member pair with  $\Delta v > 3000 \text{ km s}^{-1}$  are rejected, since such large velocity offsets are highly improbable for multiple images of a lensed quasar. After this cut, 516 out of 6 730 groups remain.

For groups that lack at least two spectroscopic measurements, we turn to photometry. Following the prescription of He et al. (2023), we calculate the colour similarity  $S_{\text{colour}}$  from the  $g$ ,  $r$ ,  $z$ ,  $W1$ , and  $W2$  fluxes and discard all groups with  $S_{\text{colour}} < 0.5$ . Each of the four discoverable known lenses in CatNorth satisfies  $S_{\text{colour}} > 0.5$ , indicating that this cut preserves real strong lenses. After applying this filter, 14 244 groups without sufficient spectroscopic information remain.

### 3.3. Human classification

After the conservative automated filtering we retain 516 groups in which at least two quasar candidate images possess optical spectra, together with 14 244 groups that lack adequate optical spectra. We subsequently conduct a visual inspection to isolate systems that are possibly WSLQs.

For the 516 groups with spectra, we first evaluated spectral similarity and the presence or absence of a foreground galaxy cluster. This examination identified two systems that are plausible WSLQs; their confirmation or refutation will require higher-quality follow-up observations. These two systems are described in Appendix A. Among the remaining groups, we applied the criteria  $\Delta v < 2000 \text{ km s}^{-1}$  and a projected distance smaller than 100 kpc, which produced 29 dual quasars detailed in Section 4.2.

For the 14 244 groups that lack adequate optical spectra, D. W. and S. C. carried out a visual inspection (VI) based on their DESI Legacy Imaging Surveys DR9 images (Zou et al. 2017; Dey et al. 2019) and Pan-STARRS1 images (Chambers et al. 2016). Before VI, the inspectors reviewed the DESI Legacy Imaging Surveys DR9 and Pan-STARRS1 images of the four discoverable known lenses to get familiar with the features of true lensed systems. During VI, each one in these 14 244 groups received a score reflecting its likelihood of being a WSLQ, based on three criteria: (i) the presence of one or more bright, colour-similar galaxies near the geometric centre of the quasar images, with preference for a luminous cD; (ii) in double-image configurations, the opening angle of the triangle defined by the putative lens and the two images, with larger angles deemed more lens-like; (iii) the degree of colour similarity among the quasar images.

Each group was then graded on a four-point scale (0, 1, 2, 3), where 0 denotes a system that is certainly not a strong lens and higher values indicate increasing probability. The final score is the average of the two inspectors' assessments. Groups with a score below 1 were discarded; the remainder were retained as WSLQ candidates, with Grade-C assigned to score 1, Grade-B to scores of 1.5 and 2, and Grade-A to scores of 2.5 and 3. This procedure yields 331 candidates, hereafter the Lensed Quasar Candidates (LQC), which is described in Section 4.1.

<sup>1</sup> When multiple spectra are available for a single member, we preferentially retain the DESI measurement, for whose deeper limiting magnitude usually provides a superior signal-to-noise ratio.

## 4. Results

In this section we first describe, in Section 4.1, the properties of lensed quasar candidates. These objects were selected through photometric colour similarity and visual inspection. Section 4.2 then presents the characteristics of the 29 dual quasars identified in this study. The two lensed quasar candidates of which spectra are available are discussed in Appendix A.

### 4.1. Lensed quasar candidates

A total of 331 lensed quasar candidates (LQC hereafter), of which 45 are classified as Grade A, 98 as Grade B, and 188 as Grade C, are identified. A cross match with existing lensed-quasar candidate catalogues (e.g., He et al. 2023; He et al. 2025; Dawes et al. 2022; Chan et al. 2023; Andika et al. 2023) yielded no counterparts, confirming that our candidates are new. Besides, to select high-value samples whose projected positions lie near galaxy clusters, a cross-match was carried out between LQC and the three galaxy cluster catalogues (WEN\_CAT, ZOU\_CAT, and ERO\_CAT) using a radius of two arcminutes. Using a cross-matching radius of two arcminutes (distance is calculated from the centre of the quasar candidates group to the Brightest Cluster Galaxy (BCG) of the galaxy cluster), which is relatively large, can improve the completeness of the cluster cross matching. 108 samples in LQC successfully matched at least one galaxy cluster in these three cluster catalogues, including 21 A grade, 30 B grade, and 57 C grade samples. The LQC and the cross matching results are summarised in a catalogue, which is online available<sup>2</sup>.

Table 2 lists the columns of our LQC catalogue: A unique groupid (identical for all members belonging to the system), R.A., Dec, VI Grade, maximum separation, number of quasar candidate members within the group, colour similarity, and crossing match results with three galaxy cluster catalogues. In addition to the parameters shown in Table 2, the online table also retains all columns provided by the original CatNorth.

Figure 3 displays five Grade-A candidates for which the BCGs of the galaxy cluster are found within 30 arcsec of the mean position of quasar candidate groups. The reason we chose 30 arcsec here is that the core region of the galaxy cluster can provide more matter density to form strong lensing, so that these would be the more promising cases. Besides, Figure 4 presents images of 15 Grade-A candidates randomly selected from the remainder of the sample, all pictures are drawn from the DESI Legacy Imaging Survey DR9. These examples illustrate that most Grade-A systems exhibit promising lens configurations and therefore constitute the high priority targets for future confirmation.

Figure 5 compares the distributions of PM\_SIG, PLX\_SIG, and the colour  $W1 - W2$ ,  $z - W1$  of the LQC, four discoverable WSLQs and a set of stars.  $PM_{\text{SIG}} \equiv \mu/\sigma_{\mu}$ , where  $\mu$  is the total proper motion and  $\sigma_{\mu}$  is its uncertainty, and  $PLX_{\text{SIG}} \equiv p/\sigma_p$ , where  $p$  is the parallax and  $\sigma_p$  is its uncertainty. The stars are drawn from Gaia DR3 (Gaia Collaboration et al. 2023b) by requiring (i) an angular distance smaller than  $3'$  from the quasar candidate group and (ii) a stellar probability  $P_{\text{star}} > 0.99$  assigned by the Discrete Source Classifier described by Gaia Collaboration et al. (2023b). By restricting the comparison stars to a small cone around each candidate (here  $< 3'$ ) in the first criterion, we ensure similar sky position, which mitigates spatially

<sup>2</sup> <https://github.com/sdwudi/Catalog-of-wide-sep-lensed-QSO-candidates-dual-QSO-from-CatNorth>

varying astrometric systematics that depend on position (Lindgren et al. 2018; Gaia Collaboration et al. 2021).

In Figure 5, the candidates occupy similar regions of parameter space as the known lenses, while the stars are clearly segregated. Specifically, in the left panel the candidates cluster at low PM\_SIG and low PLX\_SIG, as expected for extragalactic sources, whereas the stellar population forms a conspicuous sequence toward large astrometric values. In the right panel, lensed quasar candidates' ( $W1 - W2$ ,  $z - W1$ ) colours trace the discoverable lensed quasar locus and remain well separated from the stellar region. The tight overlap with known lenses and significant separation from stars in these astrometric and colour diagnostics indicate that objects in our sample are high in purity in being real quasars.

Figure 6 displays the distributions of the  $S_{\text{colour}}$ , the Pan-STARRS1  $g$  band apparent magnitude, the maximum image separation, and the photometric redshift of LQC, QGC, and discoverable quasar images in CatNorth from discoverable known lenses. Vertical dashed lines mark the information of four discoverable known lenses. The  $g$  band magnitude and redshift panels exhibit the information of all member quasar candidate images within each group of LQC and QGC; photometric redshifts are  $z_{\text{ph}}$  provided by CatNorth.

As shown in Figure 6, the  $S_{\text{colour}}$  distribution of LQC shifts toward higher colour similarity compared to QGC. This is due to the removal of groups with low colour similarity during automated filtering and the favour of colour consistency during visual inspection.

Figure 6 also shows the shift of the redshift distribution of LQC toward the low end compared to the original QGC. This has two reasons:

- 6 730 groups rejected by their spectroscopic information tend to reside at higher redshift, because the spectroscopic catalogues employed reach fainter magnitudes than *Gaia*; the redshift distribution information of this part of the samples is plotted as the blue curve in the lower-right panel of Figure 6, so the surviving sample moves to lower redshift;
- during visual inspection, brighter quasars, which are more prevalent at lower redshift, are more readily accepted because they have a higher signal-to-noise ratio, further biasing the accepted sample toward lower redshift.

We employed simple models to predict the distribution of the maximum image separation angles of lensed quasars produced by galaxy cluster lenses, in which we adopted the ellipsoidal Navarro-Frenk-White (eNFW) (Navarro et al. 1997; Guse & Kneib 2002) and Singular Isothermal Ellipsoid (SIE) models for the foreground lens. The method to generate this is described in the Appendix B. The resulting distribution (separation  $> 10$  arcsec) is plotted in the lower left panel of Figure 6. From this, we see that the peak of the separation distribution in the LQC sample is located at larger values than predicted by theory: both the SIE and eNFW model peaks between 10 and 20 arcsec, whereas the LQC sample peaks between 20 and 30 arcsec. The fractions of systems with separations exceeding 20 arcsec are approximately 25%, 35%, and 73% for eNFW, SIE, and LQC, respectively. These numbers imply that the false positive rate of LQC candidates becomes substantial at the large-separation end.

## 4.2. Dual quasars

After the subsample with spectroscopic information had been purged of likely WSLQ systems, we imposed two additional constraints that the projected separation smaller than 100 kpc

and the velocity difference below 2000 km s $^{-1}$ , which yielded a set of 29 dual quasars. The complete catalogue and the DESI legacy survey/Pan-STARRS1 images of each dual quasar are also available online. Table 3 lists the principal properties of these systems; the electronic table also contains all parameters provided by the original CatNorth, which are not exhibited in Table 3 for brevity.

Figure 8 presents cut-outs from the DESI Legacy Imaging Survey DR9 of the 29 dual quasars. Each panel spans the same angular extent of a sidelength of 30 arcsec. These image pairs either lack the evidence for the presence of enough foreground matter to form strong gravitational lensing or have clearly different spectral redshift or features, so they are confirmed to be physically associated dual quasars. Figures 7 display the optical spectra of two randomly selected systems; the upper system and lower system's velocity differences are 661.56 km s $^{-1}$  and 818.04 km s $^{-1}$ , and their projected separations are 95.01 kpc and 96.51 kpc, respectively.

Jing et al. (2025) selected 1842 quasar pairs from the DESI DR1 spectra (hereafter J25). Cross matching our 29 dualquasar candidates with J25 shows that 14 have counterparts in J25. The final table records this information in the column labelled `in_J25`, which flags whether a candidate is present in J25.

## 5. Discussion

This section is arranged as follows. Section 5.1 discusses the completeness of the WSLQ candidate sample obtained in this work. Section 5.2 analyses the proportion of two image systems within that sample. Section 5.3 introduces the planning follow-up aimed at confirming the nature of these candidates and the potential scientific significance.

### 5.1. Completeness

The completeness of the known WSLQs in CatNorth is 50 per cent, four of the eight published systems are discoverable in CatNorth. Of the remaining four, only COOL J0542–2125 (Martinez et al. 2023) has its brightest image (photometric information comes from the DESI Legacy Imaging Survey DR9, see Table 1) detected in CatNorth, whereas SDSS J2222+2745 (Dahle et al. 2013), SDSS J0909+4444 (Shu et al. 2018), and COOL J0335–1927 (Napier et al. 2023) lack any counterparts in CatNorth. The principal reason is that the magnitudes of their lensed images lie around or below the limiting magnitude of CatNorth.

The performance of the four discoverable WSLQs within our candidate-selection workflow indicates that the pre-VI stages, namely the quasar group finder and the automated screening, achieve high completeness for potential lensed quasars present in CatNorth because all four discoverable lenses successfully pass these stages.

### 5.2. Proportion of lensed quasar candidates with two image

Among the 331 lensed quasar candidate systems identified in this work, only two display three images, whereas the remaining 329 have two image counterparts in CatNorth. This proportion of two image systems is much higher than the proportion of doubles in the set of eight published WSLQs, where only SDSS J1326 + 4806 is a double image system. Two factors seem to account for the difference: the limiting magnitude of

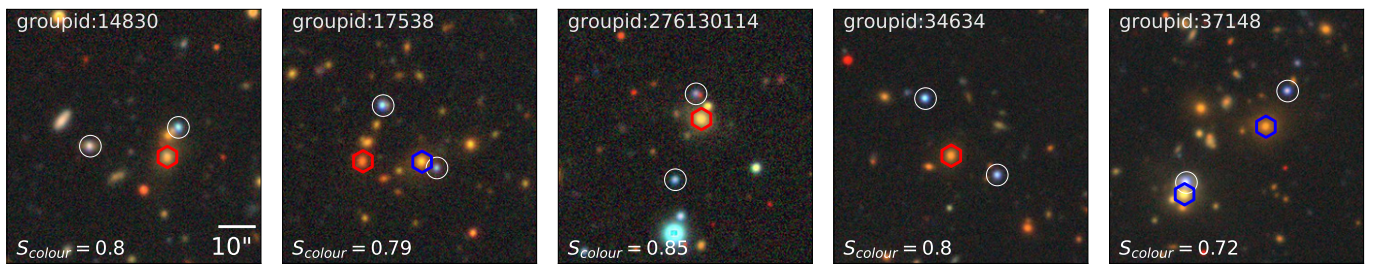


**Fig. 3.** DESI Legacy Imaging Surveys DR9  $grz$  composite images of the five Grade-A candidates for which at least one galaxy cluster is located within 30 arcsec of the quasar group centre. Each image spans 70 arcsec  $\times$  70 arcsec. White circles indicate the quasar candidate images, while red and blue circles mark the positions of the BCG matched in WEN\_CAT and ZOU\_CAT, respectively.

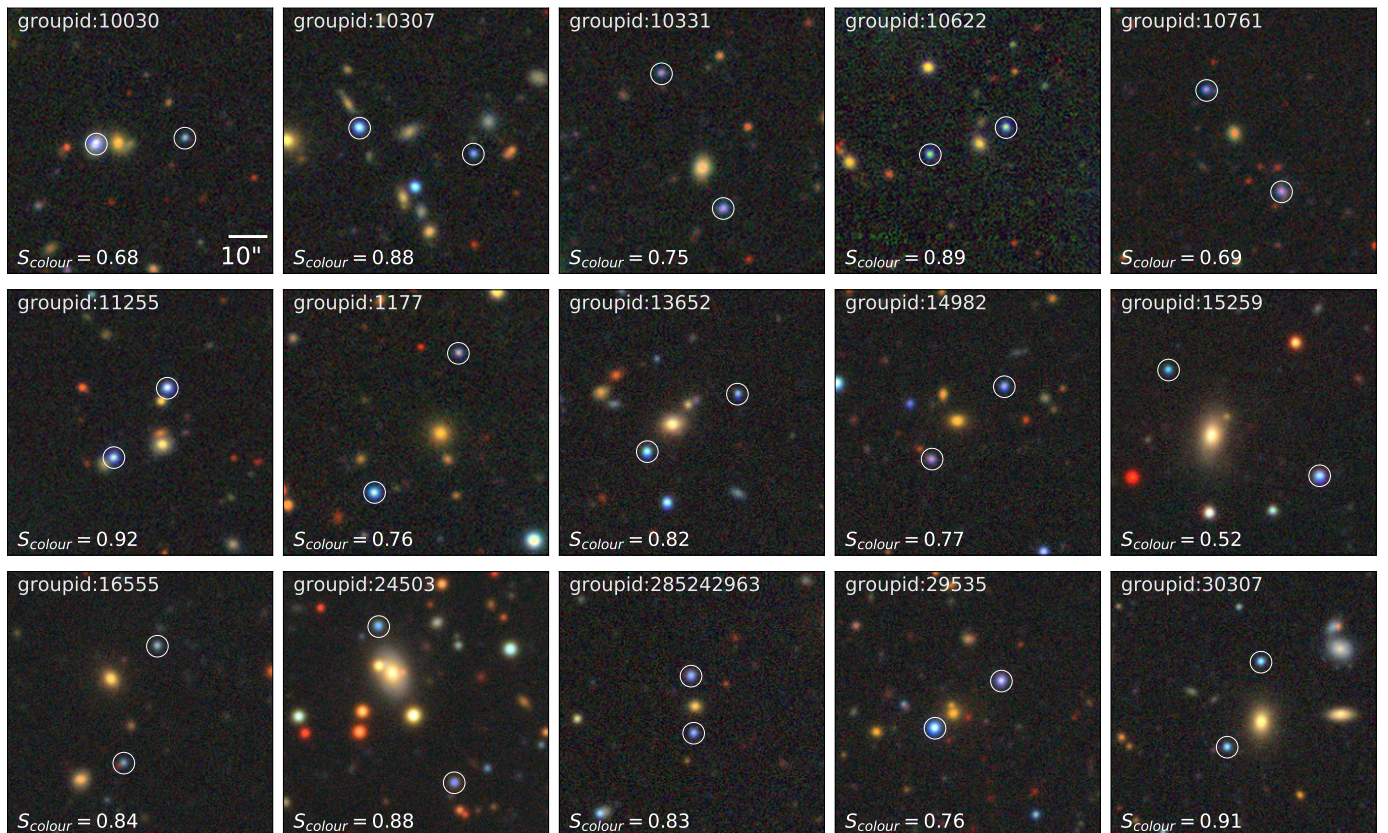


**Fig. 4.** DESI Legacy Imaging Surveys DR9  $grz$  composite images of the first fifteen Grade-A candidates for which no galaxy cluster is matched within 30 arcsec of the quasar group centre. Each panel spans 70 arcsec  $\times$  70 arcsec. White circles mark the positions of the quasar candidate images.

*Gaia/CatNorth* and the non-zero probability that the *CatNorth* construction process removed one or more true quasar images. These factors likewise explain why each of the three discoverable known lenses present in *CatNorth*, i.e. J1004 + 4112, SDSS J1029 + 2623, and GraL J165105.3 – 041725, which possess four, three, and four images respectively, appear with only two image counterparts recorded in *CatNorth*. Consequently, any as-yet-unknown positive systems that can be detected in *CatNorth* are likely to be represented by no more than two images.

### 5.3. Follow-up and scientific significance

We plan to carry out follow-up confirmation of the strong lensing candidates identified in this study, employing distinct verifica-

tion strategies tailored to each class of candidate. For the high quality lensed quasar candidates in Grade-A, especially those that can be matched with galaxy clusters, we plan to request observing time on the Canada-France-Hawaii Telescope (CFHT) and the 200-inch Hale Telescope (P200) to obtain deep imaging and spectroscopic observations. High signal-to-noise spectra will permit the rejection of obvious contaminants, while deeper imaging that resolves arcs or other multiple images will provide additional constraints on the mass distribution in the lensing region. For the samples which already have spectral information, we intend to apply for deeper imaging observations. For the remaining lensed quasar candidates, we will cross-match with DESI future release spectroscopy, and as public releases expand Euclid imaging/slitless spectroscopy, future survey observations on the 4-metre Multi-Object Spectroscopic Telescope (4MOST)

**Table 2.** Column description of the WSLQ candidate catalogue (LQC).

Col.	Name	Type	Unit	Description
1	ra	double	deg	Gaia DR3 right ascension (ICRS, epoch 2016.0)
2	dec	double	deg	Gaia DR3 declination (ICRS, epoch 2016.0)
3	groupid	int	—	Candidate lens system identifier
4	Grade	string	—	System grade (A, B, or C)
5	sep_max	float	arcsec	Maximum angular separation between quasar members
6	z_diff	float	—	Maximum $\Delta z_{\text{ph}}$ among members
7	quasar_num	int	—	Number of quasar members
8	S_colour	float	—	Colour-similarity statistic
9	Wen_BCG_RA	float	deg	R.A. of matched BCG in WEN_CAT
10	Wen_BCG_DEC	float	deg	Dec. of the same BCG
11	Wen_redshift	float	—	Cluster redshift in WEN_CAT
12	Wen_M500	float	$10^{14} M_{\odot}$	$M_{500}$ in WEN_CAT
13	Wen_ID	int	—	Cluster identifier in WEN_CAT
14	Zou_BCG_RA	float	deg	R.A. of matched BCG in ZOU_CAT
15	Zou_BCG_DEC	float	deg	Dec. of the same BCG
16	Zou_redshift	float	—	Cluster redshift in ZOU_CAT
17	Zou_M500	float	$\log_{10}(M_{\odot})$	$M_{500}$ in ZOU_CAT
18	Zou_ID	int	—	Cluster identifier in ZOU_CAT
19	eROSITA_RA	float	deg	R.A. of matched eROSITA cluster
20	eROSITA_DEC	float	deg	Dec. of the same cluster
21	eROSITA_redshift	float	—	eROSITA cluster redshift
22	eROSITA_M500	float	$10^{13} M_{\odot}$	$M_{500}$ in eROSITA catalogue
23	eROSITA_ID	int	—	Cluster identifier in eROSITA catalogue

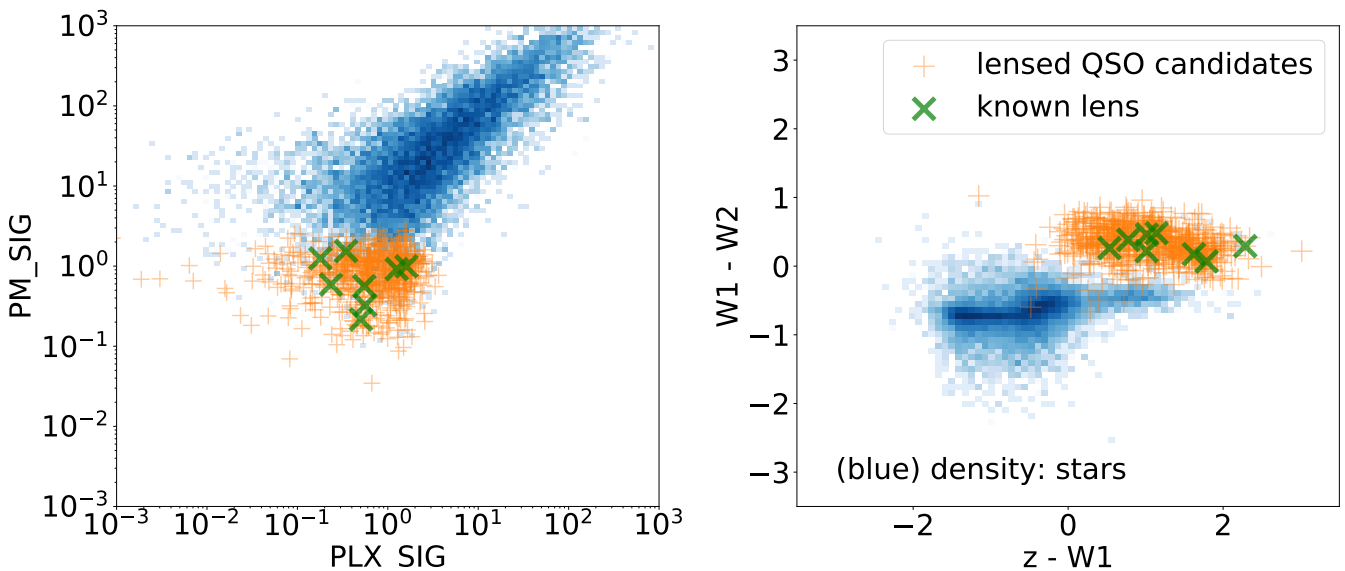


**Fig. 5.** The distribution of the properties of the LQC (orange plus signs), the eight images of the four discoverable known lenses in CatNorth (green cross symbols), and the stellar population located within  $3'$  of all LQC objects (blue density map). *Left:* two-dimensional distribution of total PM\_SIG (the absolute value of the proper motion divided by its uncertainty) versus PLX\_SIG (the absolute value of the parallax divided by its uncertainty). *Right:* two-dimensional distribution of the  $W_1 - W_2$  and  $z - W_1$ , which is defined in AB magnitude system. We want to note that WISE photometry is calibrated in the Vega system. We convert to AB using  $m_{\text{AB}} = m_{\text{Vega}} + \Delta m$ , with  $\Delta m_{W_1, W_2} = (2.699, 3.339)$ , given by [Cutri et al. \(2013\)](#).

and the forthcoming CSST imaging/slitless spectroscopy wide-field surveys when data is available.

If confirmed, these candidates would offer substantial scientific value. For instance, within the subset (shown in Figure 3) where the BCG of a galaxy cluster lies within 30 arcsec of the quasar-group centre, the rightmost panel of Figure 3 shows the candidate with  $groupid = 37148$ , whose image separation is 37.59 arcsec-exceeding that of all currently known WSLQs. If genuine, its large separation would provide a uniquely valuable case for probing the three-dimensional structure of quasars ([Misawa et al. 2016](#)).

As another example, Appendix A.2.1 discusses a candidate in which the mass centroid and luminosity centroid may be offset; if verified, this system would be highly informative for constraining the mass distribution of this irregular foreground galaxy cluster.

## 6. Conclusion

In this work, the catalogue-based searching strategy of [He et al. \(2023\)](#) is applied to CatNorth, a high purity and highly com-

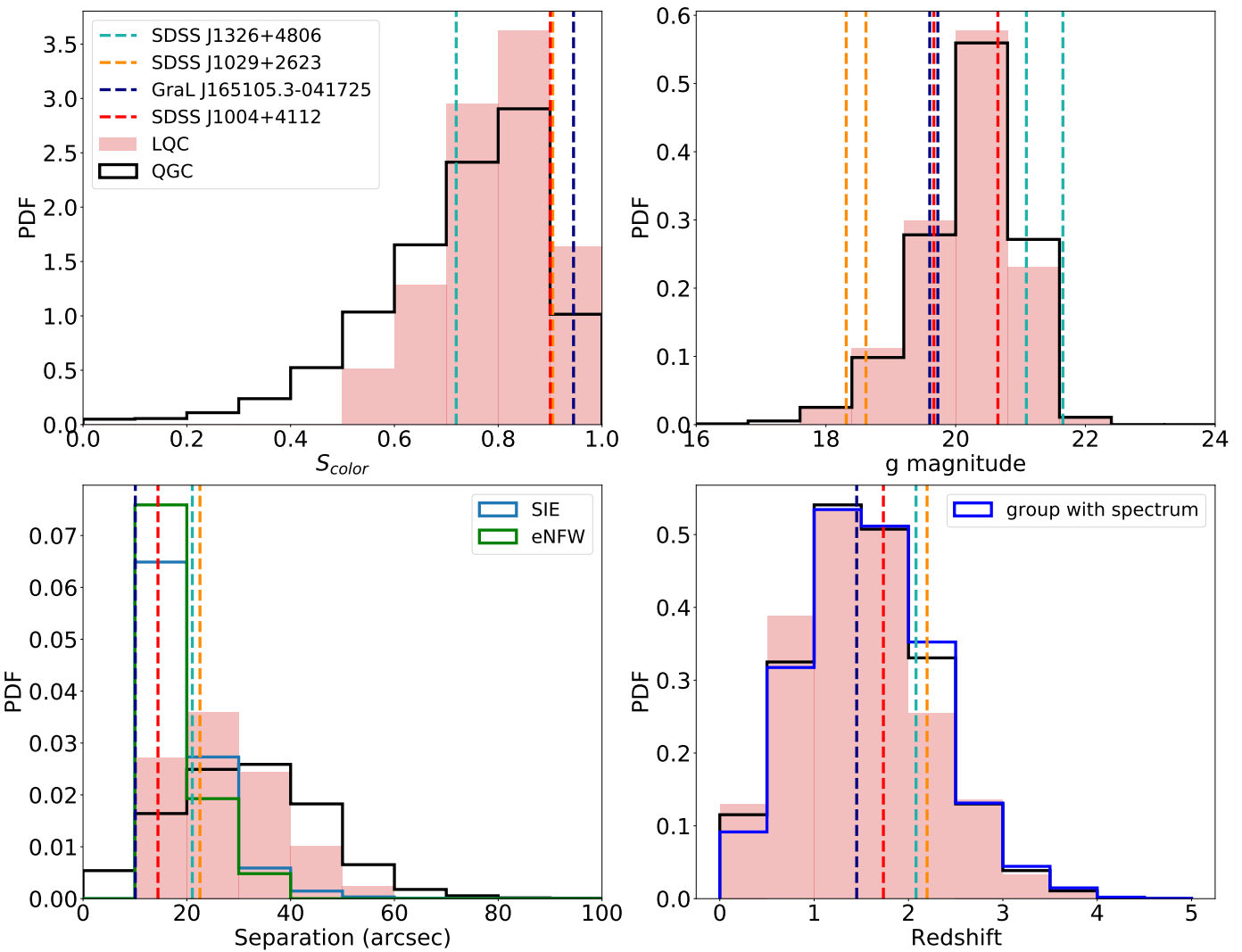


**Fig. 6.** Statistical properties of LQC, QGC, and discoverable known lenses. Upper left: distribution of the colour similarity  $S_{\text{colour}}$ . Upper right: distribution of the Pan-STARRS1  $g$  band magnitudes for all quasar images contained in each quasar candidate group or known lensed quasar system. Lower left: distribution of the maximum image separation. The blue and green curves are the simulation results derived from the model in Appendix B, corresponding to different lens mass profile models. Lower right: distribution of the photometric redshift  $z_{\text{ph}}$  for all quasar images in each group or known system; the blue curve shows the  $z_{\text{ph}}$  distribution for those quasar candidate groups in the Quasar Group Catalogue (QGC) that have sufficient spectroscopic matches. Dashed lines indicate the positions of the corresponding values for the four discoverable known lenses in CatNorth. Black stepped histograms trace the distributions for the QGC.

plete quasar candidate catalogue derived from *Gaia* DR3, to search for WSLQ candidates. The analysis delivers and releases two samples: a set of WSLQ candidates and a set of dual quasars. The procedure consists of three steps. (i) The group finder is run on the 1 545 514 quasars and generates about 24 000 quasar groups. (ii) These groups are filtered by their colour properties or by spectra retrieved from SDSS DR16 and DESI DR1, this operation reduces the sample to about 14 000 groups. (iii) Visual inspection assigns scores and categories to the surviving systems and removes those that are very likely to be spurious.

The resulting WSLQ candidate sample contains two systems for which spectroscopic data are available and 331 systems selected solely on the basis of colour and imaging information in the absence of adequate spectroscopy. The two systems with spectroscopic records have been subjected to spectral analysis and preliminary lens modelling to estimate the foreground mass required if they are real strong lenses. The 331 colour-selected candidates were scored and placed into three classes: 45 Grade-

A, 98 Grade-B, and 188 Grade-C. The complete sample has been cross matched with roughly 1.9 million galaxy clusters and groups. 108 samples successfully matched at least one galaxy cluster within 2 arcmin in three cluster catalogues which we used, and the result is included in the publicly available table.

Applying the additional criteria of a velocity difference  $\Delta v < 2000 \text{ km s}^{-1}$  and a projected separation smaller than 100 kpc on the remaining quasar candidate groups whose spectra are available yields a catalogue of 29 dual quasars. Their images show the lack of evidence of the image morphology and spectrum characteristic of strong lensing, but their small line-of-sight velocity separations suggest that they satisfy conventional criteria for the dual quasar.

We plan to obtain supplementary spectroscopy and deep imaging for the candidates identified in this study using CFHT, P200, and DESI future release, while the ongoing and forthcoming wide-field surveys with Euclid and CSST will aid the confirmation of lensed quasars in the long term. Spectroscopic obser-

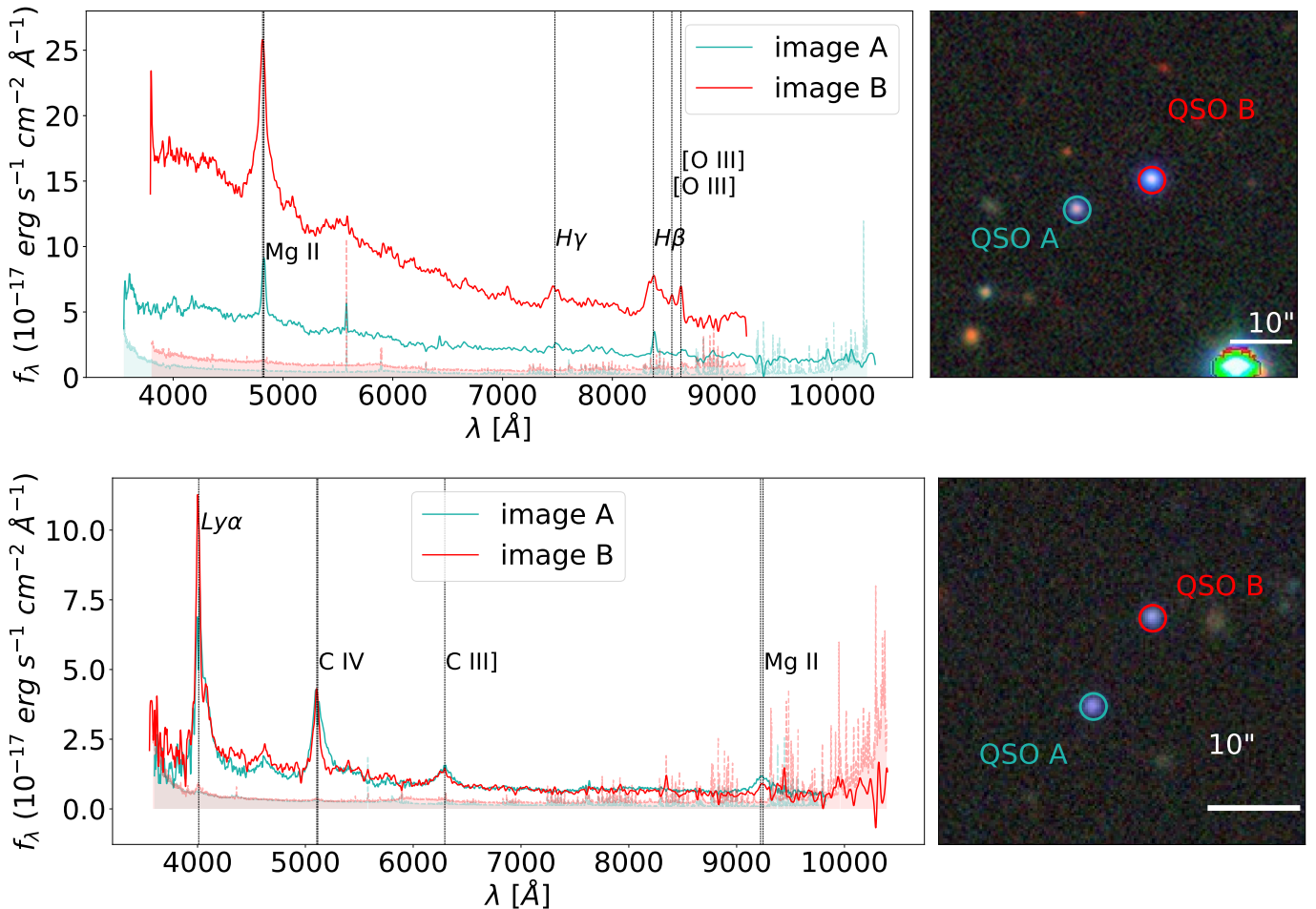


**Fig. 7.** Spectra and images of two dual quasars. In each row the left subpanel shows the spectra and the right subpanel presents the DESI Legacy Imaging Surveys DR9 grz composite image. *Top:* dual quasar of groupid = 9333. Spectrum of image A is from SDSS DR16 and that of image B is from DESI DR1; automated spectral redshifts are  $z_A = 0.7239$  and  $z_B = 0.7201$ . The angular separation is 13.17 arcsec, corresponding to a projected distance of 95.01 kpc; the velocity difference is 661.56 km s $^{-1}$ . *Bottom:* dual quasar of groupid = 26644. Spectrum of image A derives from DESI DR1 and image B from SDSS DR16 with automated spectral redshifts  $z_A = 2.3028$  and  $z_B = 2.2938$ . The angular separation is 11.61 arcsec, giving a projected distance of 96.51 kpc; the velocity difference is 818.04 km s $^{-1}$ .

inations will refine the sample by confirming plausible strong lens systems and discarding obvious contaminants, whereas deeper imaging will reveal additional strong lensing indicators and impose tighter constraints on the mass distribution of the foreground deflectors. Together, these data are essential for establishing the physical nature of the candidates.

In summary, we have implemented a robust pipeline that starts from the quasar candidate catalogue CatNorth and produces a catalogue of WSLQ candidates together with a catalogue of dual quasars; lens modelling has been carried out for the two high-quality systems whose spectroscopic information is available. Follow-up spectroscopy and deep imaging of the most promising candidates are planned to confirm new WSLQs based on these samples in the near future. The present study also demonstrates that the proposed automated procedure can markedly compress a very large parent sample of quasar candidates while maintaining high completeness, an ability that will be invaluable for efficiently selecting WSLQs in the next-generation deep, wide-field imaging surveys.

**Acknowledgements.** We thank astropy, HEALPix, pandas, and lenstronomy for providing convenient and reliable Python packages. We thank Yiping Shu for insightful discussions. Z.H. acknowledges support from a fellowship of the China Postdoctoral Science Foundation (Certificate Number: 2025T180871) and the

National Natural Science Foundation of China (Grant No. 12403104). N.L. acknowledges the support of the science research grants from the China Manned Space Project (No. CMS-CSST-2021-A01) and the CAS Project for Young Scientists in Basic Research (No. YSBR-062). We thank ChatGPT for polishing the English in this paper.

**Table 3.** Column description of the dual quasars catalogue.

Col.	Name	Type	Unit	Description
1	ra	double	deg	Gaia DR3 right ascension (ICRS, epoch 2016.0)
2	dec	double	deg	Gaia DR3 declination (ICRS, epoch 2016.0)
3	groupid	int	—	Dual quasar system identifier
4	dv	float	$\text{km s}^{-1}$	Line-of-sight velocity difference
5	sep_max	float	arcsec	Maximum angular separation of the pair
6	dis	float	kpc	Maximum projected separation
7	Wen_BCG_RA	float	deg	R.A. of matched BCG in WEN_CAT
8	Wen_BCG_DEC	float	deg	Dec. of the same BCG
9	Wen_redshift	float	—	Cluster redshift in WEN_CAT
10	Wen_M500	float	$10^{14} \text{ M}_\odot$	$M_{500}$ from WEN_CAT richness
11	Wen_ID	int	—	Cluster identifier in WEN_CAT
12	Zou_BCG_RA	float	deg	R.A. of matched BCG in ZOU_CAT
13	Zou_BCG_DEC	float	deg	Dec. of the same BCG
14	Zou_redshift	float	—	Cluster redshift in ZOU_CAT
15	Zou_M500	float	$\log_{10}(\text{M}_\odot)$	$M_{500}$ in ZOU_CAT
16	Zou_ID	int	—	Cluster identifier in ZOU_CAT
17	eROSITA_RA	float	deg	R.A. of matched eROSITA cluster
18	eROSITA_DEC	float	deg	Dec. of the same cluster
19	eROSITA_redshift	float	—	eROSITA cluster redshift
20	eROSITA_M500	float	$10^{13} \text{ M}_\odot$	$M_{500}$ in eROSITA catalogue
21	eROSITA_ID	int	—	Cluster identifier in eROSITA catalogue
22	in_J25	flag	—	Whether this dual quasar exists in J25

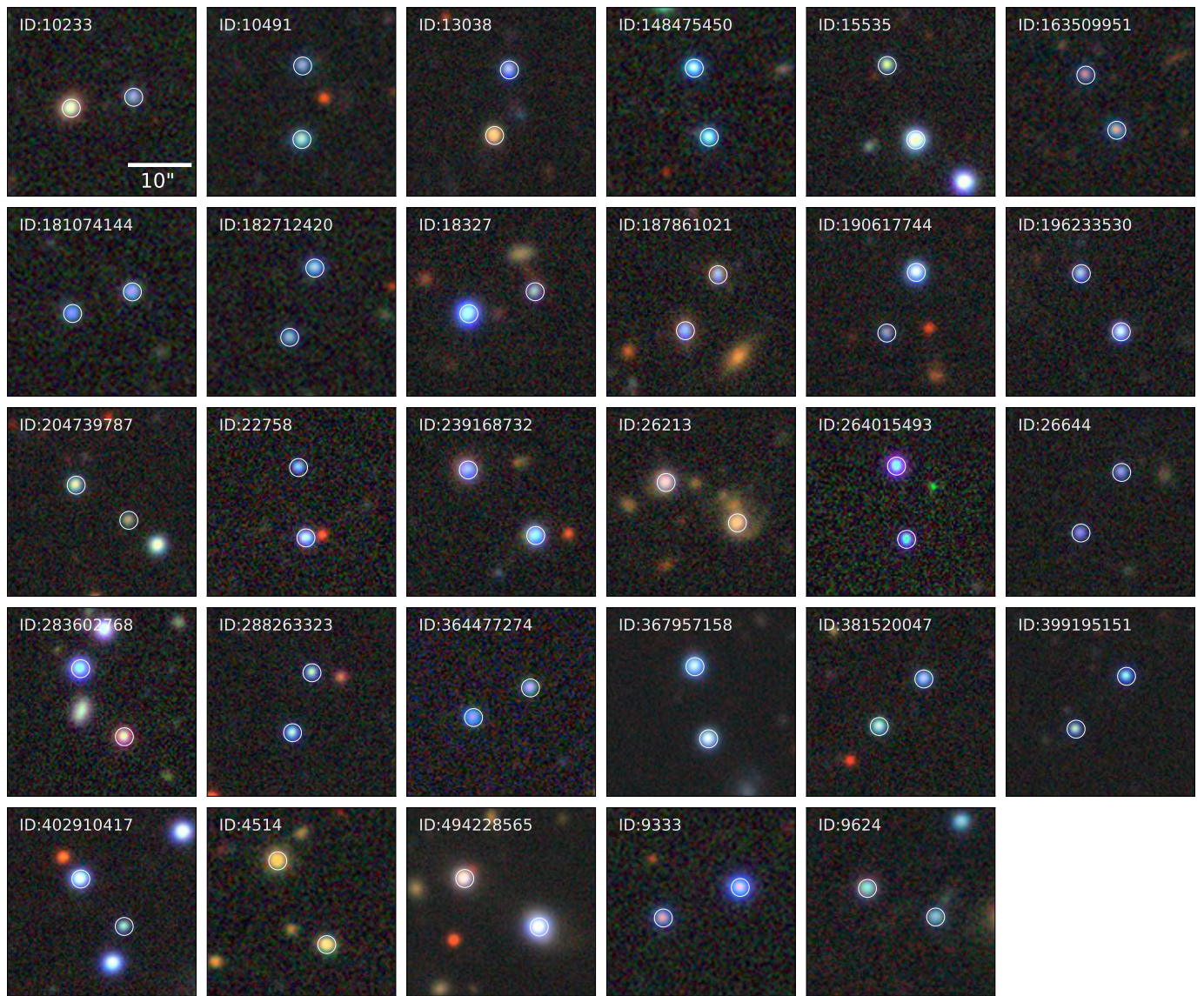


**Fig. 8.** DESI Legacy Imaging Surveys DR9  $grz$  composite images of the 29 dualquasar candidate systems. Each cut-out spans 30 arcsec  $\times$  30 arcsec. White circles mark the positions of the quasar candidate images.

## Appendix A: Candidates with spectrum

Spectroscopic observations of quasars are invaluable for excluding systems that are not real strong lenses. Microlensing (Sluse et al. 2012; Motta et al. 2012; Hutsemékers et al. 2023), variability in the broad emission lines and continuum (Shen et al. 2019), differential reddening, differences in sight-line (Misawa et al. 2016) can introduce differences between the spectra of multiple images. Nevertheless, the spectra of confirmed strong-lens systems are, in an overall sense, highly similar, and any systematic discrepancies can be attributed to the effects listed above.

This section discusses two systems with spectroscopical information that are plausible strong lenses and presents their lens modelling process. Section A.1 outlines the modelling methodology, whereas Section A.2 describes the information of two candidate strongly lensed quasars and the corresponding modelling results.

### Appendix A.1: Lens modelling methodology

In our lens modelling methodology the foreground lens is represented with a singular isothermal ellipsoid (SIE) mass profile. The model contains three free parameters: the velocity dispersion  $\sigma_v$ , the axis ratio  $q$ , and the position angle  $\phi$  of the major axis of the mass contour. Deflection angles and image positions are computed with the `lenstronomy` package (Birrer & Amara 2018; Birrer et al. 2021), and the parameter posterior is sampled by the Markov chain Monte Carlo ensemble sampler `emcee` (Foreman-Mackey et al. 2013). The likelihood is built from the positional offsets between the model quasar image and the observations,

$$\chi_{\text{pos}}^2 = \sum_i \frac{|\mathbf{r}_i^M - \mathbf{r}_i|^2}{\sigma_i^2}, \quad (\text{A.1})$$

where  $\mathbf{r}_i^M$  and  $\mathbf{r}_i$  are the modelled and observed positions of the  $i$ th image, and  $\sigma_i$  is the corresponding astrometric uncertainty.

The SIE profile offers the advantage of a small parameter set, which limits degeneracies when only a few image positions

are available. Its simplicity, however, makes it an imperfect description of cluster scale haloes, whose central density profiles are usually flatter and often require multiple subhaloes for an accurate modelling (Sharon et al. 2020). But given the limited observational constraints presently available for the candidates discussed here, the SIE model provides a useful first approximation; more elaborate mass models should be adopted once deeper imaging and additional spectroscopy become accessible.

### Appendix A.2: Samples

#### Appendix A.2.1: J110121.67+060931.3

Two quasar images in this system have similar spectral features, and a foreground galaxy cluster acts as a plausible deflector. The spectra and DESI Legacy Imaging Surveys DR9 image of this system are displayed in Figure A.1, left and right panels respectively. Images A and B are separated by 14.14 arcsec. In the uppermost panel of the spectral figure, the spectrum is convolved with a scale kernel whose width is five pixels for smoothing. Both spectra originate from DESI-DR1, automatic DESI-DR1 redshift fits yield  $z_A = 0.8313 \pm 0.0001$  and  $z_B = 0.8297 \pm 0.0002$ . The spectrum of image A is of lower quality and exhibits numerous spurious absorption features with zero signal-to-noise (for example near 5907 Å), introduced when zero-filled regions were convolved with neighbouring valid data. Image B appears slightly redder than image A, and the continuum flux ratio varies with wavelength; these differences may arise from differential reddening, microlensing, and intervening line-of-sight structure.

A foreground galaxy cluster is matched in WEN\_CAT, and an X-ray signal is recorded in *eRASS1 Main catalogue* (Merloni et al. 2024), which is the possible X-ray emission from the hot gas of this galaxy cluster. The BCG is marked by the white circle north of the quasar images in Figure A.1. WEN\_CAT lists a photometric redshift  $z_{\text{ph}} = 0.2503$  and  $M_{500} = 5.0 \times 10^{13} M_{\odot}$  of this cluster. A recorded X-ray signal from the *eRASS1 Main catalogue* (Merloni et al. 2024) is located at the yellow triangle in Figure A.1. The position uncertainty of this X-ray signal in *eRASS1 Main catalogue* is 2.41 arcsec; the offset between this X-ray signal and image A is 4.264 arcsec, corresponding to 1.77 X-ray signal position uncertainty, so the emission has an opportunity to originate from quasar image A too. The 0.2 - 2.3 keV flux of this X-ray signal is  $1.86 \times 10^{-13} \text{ erg s}^{-1} \text{ cm}^{-2}$ . Adopting this value as a lower limit for the galaxy cluster yields a luminosity lower limit of  $2.95 \times 10^{43} \text{ erg s}^{-1}$ . Using the empirical mass luminosity relation of Reiprich & Böhringer (2002) for the 0.1 - 2.4 keV band gives  $M_{500} \gtrsim 2 \times 10^{14} M_{\odot}$ .<sup>3</sup>

Lens modelling of this system follows the methodology outlined in Section A.1. Two centring hypotheses are examined. In the first, the BCG is adopted as the centre of the mass model; under this assumption a configuration with only two quasar images cannot be reconciled with the observations, and a search of the DESI Legacy Imaging Surveys DR9 image reveals no additional quasar images in the regions where three- or four-image configurations would place them. In the second hypothesis the centre of the mass distribution is taken to coincide with the peak of the X-ray emission. Under this assumption the observed quasar images are well reproduced by the SIE model. The best fit gives  $\sigma_v = 608.58 \text{ km s}^{-1}$ ,  $q = 0.89$ , and  $\phi = 19.32^\circ$ . The left panel of Figure A.3 displays the corresponding lens model.

<sup>3</sup> K-correction is neglected; for galaxy clusters with  $kT=0.5 - 10 \text{ keV}$  at  $z = 0.25$ , the K-correction affects the luminosity by 0 to about 13 per cent (Böhringer et al. 2004).

Following the galaxy cluster mass estimation framework used in [Shu et al. \(2019\)](#), we estimate the mass of the second lens model assumption as follows, and found that the mass inferred based on X-ray observation is compatible with the lens model and is sufficient to generate the observed lensed quasar images separation. The Einstein radius of this lens model is 7.187 arcsec, which implies an enclosed mass of  $7.394 \times 10^{12} M_{\odot}$  within Einstein radius. For an NFW halo with a lower mass limit of  $2 \times 10^{14} M_{\odot}$  (given by x-ray observation in this sample) and concentration  $3 \leq c \leq 8$ , the projected mass within  $R < 7.187$  arcsec has a lower mass limit which lies in the range  $(2.31-5.33) \times 10^{12} M_{\odot}$ , consistent with the value derived from the lens model. If the estimation  $M_{500} = 5 \times 10^{13} M_{\odot}$  provided by WEN\_CAT is adopted, where the  $M_{500}$  is given by the richness, the projected mass inside the same radius is insufficient to produce an Einstein radius as large as 7.187 arcsec.

We want to note that all eight known WSLQs can be satisfactorily fit with cluster mass centroids that nearly coincide with the BCG. Nevertheless, a non-negligible displacement between the cluster centre of mass and the BCG is still permitted by the data, leaving the second lens modelling hypothesis possible. Some studies find significant offsets between the hot gas peak and the central galaxy in a fraction of clusters ([Zhang et al. 2019](#); [Lauer et al. 2014](#); [Sehgal et al. 2013](#); [Ding et al. 2023](#)). For example, [Lauer et al. \(2014\)](#) find that in the sample of 433 BCGs with redshift smaller than 0.08 about fifteen per cent have an X-ray-BCG offset exceeding 100 kpc. [Ding et al. \(2023\)](#) show that among 186 clusters with  $0.1 \leq z \leq 1.4$ , approximately 25 per cent have a central galaxy-SZ offset larger than 330 kpc, although refining the BCG identification reduces this fraction to about ten per cent. The same study reports that within a radius of 0.3 to 1 Mpc clusters with small offsets exhibit considerably stronger lensing signals than clusters with large offsets. These results indicate that the central galaxy is not always a reliable indicator of the gravitational potential centre.

Further confirmation or refutation of this candidate requires deeper multi-wavelength imaging to pinpoint the cluster mass centroid and profile more accurately or to reveal fainter quasar image candidates below the DESI Legacy Imaging Surveys DR9 detection limit that would support a model centred on the BCG or another location.

#### Appendix A.2.2: J150155.61-025728.4

Figure A.2 shows the spectra (left panel) and the DESI Legacy Imaging Surveys DR9 image (right panel) of this system. The separation between images A and B is 19.32 arcsec. In the upper left panel, the spectrum convolve scale uses a kernel of five pixels. Both spectra are from DESI DR1, which yields automatic redshifts  $z_A = 1.6438 \pm 0.0004$  and  $z_B = 1.6475 \pm 0.0002$ .

The DESI Legacy Imaging Surveys DR9 image shows that a galaxy cluster or group possibly existed between images A and B. The brightest object situated between the two quasar images is a star. A galaxy immediately to its north has a spectroscopic redshift of 0.89 in DESI DR1. Two fainter red objects located west and northeast (close to image B) of this galaxy have photometric redshifts of  $0.921 \pm 0.075$  and  $0.923 \pm 0.17$  in the DESI Legacy Imaging Surveys DR9 catalogue. These three images are indicated by white circles in Figure A.2. These measurements suggest that a galaxy group or cluster at  $z \simeq 0.89$  may reside in the central region and provide the gravitational potential necessary to produce the double quasar images. Deeper imaging will be required to confirm or rule out this possibility.

The spectra of images A and B have some different features, which can not rule out the possibility of this system being a real lensing system, because these might be attributed to several mechanisms. For example, the ratio of the red to blue wings of the Mg II and C III] lines in image B differs markedly from that in image A. Such a difference could arise from microlensing. [Sluse et al. \(2012\)](#); [Motta et al. \(2012\)](#); [Hutsemékers et al. \(2023\)](#) reported cases in which microlensing selectively amplifies one wing (either blue or red) of a broad emission line in a lensed quasar system. At the position of C IV in image A, and on the blue wing of C IV in image B, multiple different narrow absorption lines (NALs) are present; these could represent intrinsic outflow absorbers that differ between the sightlines of the two images. [Misawa et al. \(2016\)](#) observed significant variations in intrinsic NALs between images of WSLQs that sample different sightlines. An alternative possibility is that some of these narrow absorption features originate in intervening material which is unrelated to the quasar.

Applying the lens modelling method outlined in Section A.1, the system was successfully modelled with a SIE mass profile. The lens centre was fixed at the object with spectroscopic redshift  $z = 0.89$  located north of the bright star. The model reproduces the observed configuration well: the best-fitting value gives  $\sigma_v = 988.96 \text{ km s}^{-1}$ ,  $q = 0.98$ ,  $\phi = 29.19^\circ$ , an Einstein radius of 9.364 arcsec, and a projected mass within that radius of  $5.503 \times 10^{13} M_{\odot}$ . The best-fitting result is shown in the right-hand panel of Figure A.3.

Confirmation or refutation of this candidate demands deeper imaging and additional high quality spectroscopy. Deeper data may uncover neighbouring strong-lensing features, allowing a more reliable estimate of the lens galaxy cluster properties, particularly its mass. Multiple spectroscopic observations of the quasar images will help to determine whether the observed spectral differences are produced by microlensing, differential absorption, or other mechanisms.

## Appendix B: Simulating multi-image maximum separation distribution

We employed Monte Carlo simulation to predict the distribution of the maximum image angular separation of lensed quasars produced by galaxy cluster lenses, the relevant result is shown in Figure 6. The simulation comprises three parts: a foreground light cone, a background light cone, and the lensing simulation.

For the deflectors in the foreground light cone we adopt the cluster redshifts, masses, and sky coordinates provided by the ZOU\_CAT, but assign halo ellipticities through a Monte Carlo procedure. Which incorporates redshift evolution: we set the ellipticity distribution at  $z = 0$  to have a mean  $\bar{e} = 0.33$  ([Hopkins et al. 2005](#)) and standard deviation  $\sigma_e = 0.16$  ([Plionis et al. 1991](#)), and let the mean evolve as  $\bar{e} = 0.33 + 0.05z$  ([Hopkins et al. 2005](#)), and assume  $\sigma_e$  does not evolves along redshift ([Allgood et al. \(2006\)](#) and [Suto et al. \(2016\)](#) show that  $\sigma_e$  differs small in the redshift range 0 to 3 and 0 to 1, respectively); the position angle of the major axis is drawn from a uniform distribution. We assume two alternative mass models for the foreground haloes, SIE and eNFW; for the latter, the concentration parameter is computed from the fitting formulae of [Child et al. \(2018\)](#), while the nonlinear (collapse) mass scale  $M_{\star}$  is calculated with the public Python package COLOSSUS ([Diemer 2018](#)).

The background quasar population is likewise generated by Monte Carlo sampling: source redshifts follow the quasar redshift distribution of CatNorth, whereas their sky positions are assumed to be uniformly distributed.

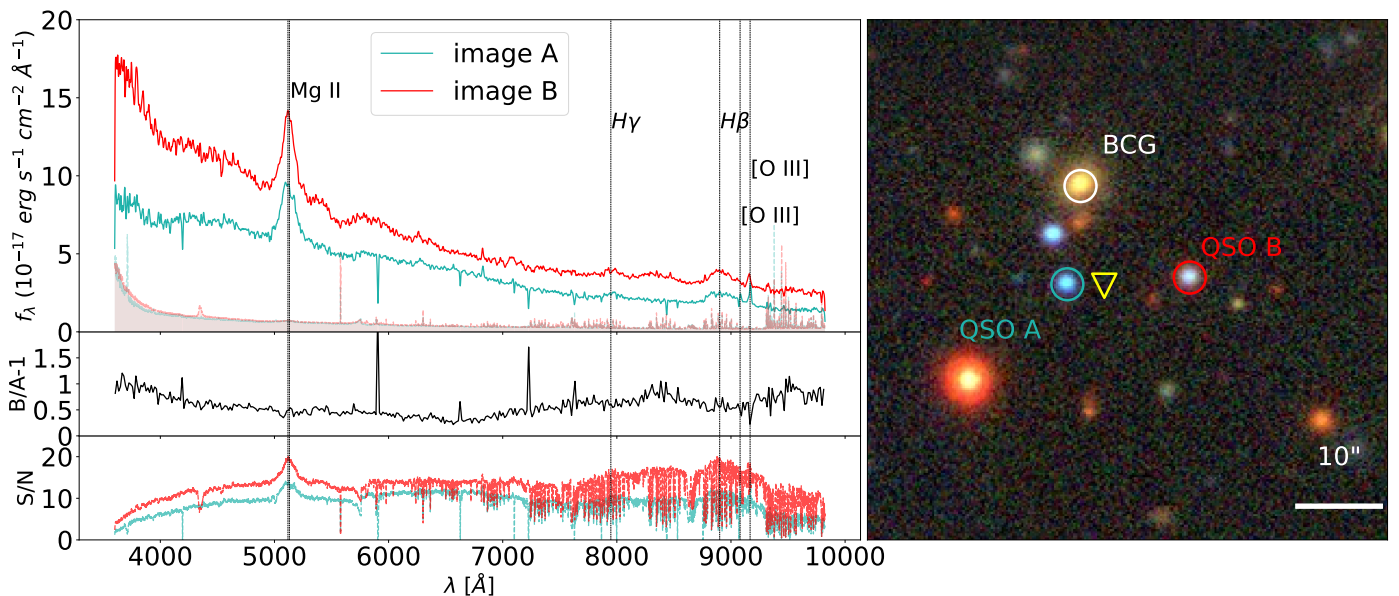


**Fig. A.1.** Spectra and DESI Legacy Imaging Surveys DR9 images of J110121.67+060931.3. Left column, top: DESI DR1 spectra of images A and B, each curve smoothed with a five-pixel kernel for clarity; the shaded regions represent the unsmoothed noise. Left column, middle:  $(F_A/F_B) - 1$ , where  $F_A$  and  $F_B$  are the smoothed flux densities of images A and B, respectively. Left column, bottom: signal-to-noise ratios of images A and B, calculated as the smoothed flux divided by the unsmoothed noise. Vertical reference spectral lines correspond to redshift  $z = 0.8305$ . Right panel: DESI Legacy Imaging Surveys DR9  $grz$  composite image of the system. The white circle marks the BCG position obtained from the WEN\_CAT cross-match, and the yellow inverted triangle marks the X-ray source position matched in the *eRASSI Main catalogue* (Merloni et al. 2024).

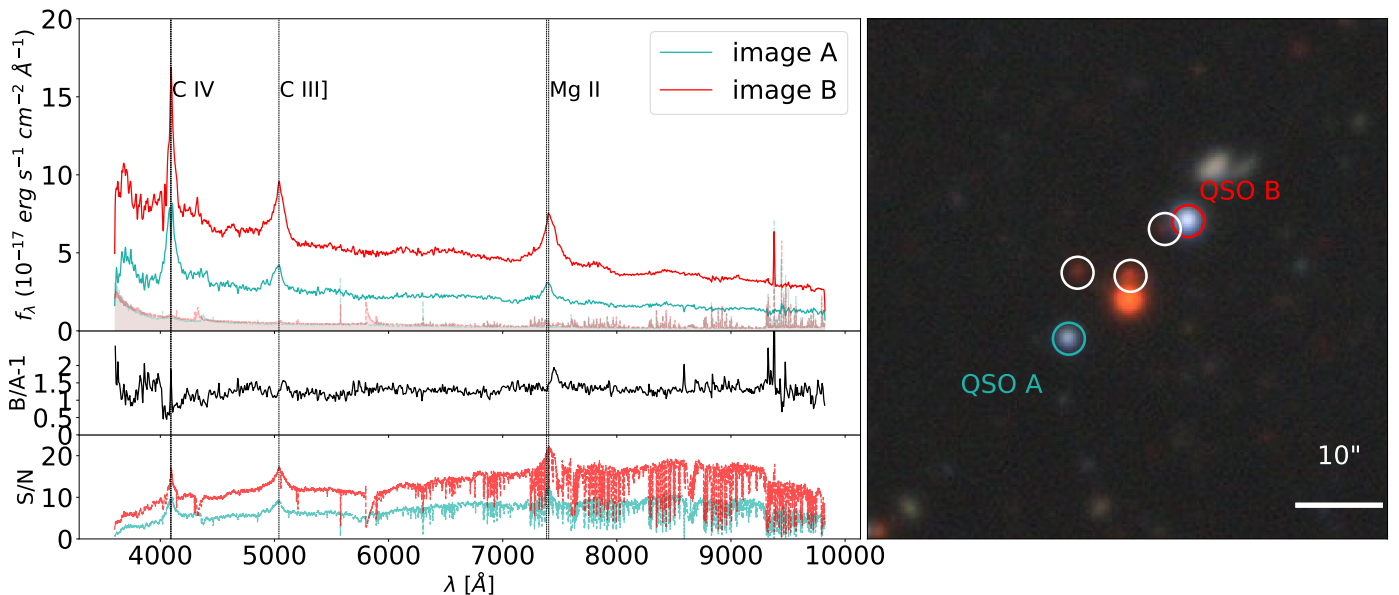


**Fig. A.2.** Spectra and DESI Legacy Imaging Surveys DR9 image of J150155.61-025728.4. Left column, top: DESI DR1 spectra of images A and B, each smoothed with a five-pixel kernel for clarity; shaded regions show the unsmoothed noise. Left column, middle:  $(F_A/F_B) - 1$ , where  $F_A$  and  $F_B$  are the smoothed flux densities of images A and B, respectively. Left column, bottom: signal-to-noise ratios of images A and B, calculated as the smoothed flux divided by the unsmoothed noise. Vertical reference lines correspond to a redshift of  $z = 1.64565$ . Right panel: DESI Legacy Imaging Surveys DR9  $grz$  composite image of the system. The brightest central object is a star. Immediately to its north lies a galaxy with a spectroscopic redshift  $z = 0.89$ . Two red galaxies located west and northeast (near image B) of this galaxy have photometric redshifts  $0.921 \pm 0.075$  and  $0.923 \pm 0.17$ , respectively. These data suggest that a galaxy group or cluster at  $z \approx 0.89$  may reside between the two quasar images.

Based on the foreground light cone and the background quasar population, we perform the lensing simulation to generate the multi-image separation distribution. During the lensing simulation, mock quasars are treated as point sources. For each of the sources, we include all foreground haloes within  $100''$  of the quasar and use the `lenstronomy` package (Birrer & Amara

2018; Birrer et al. 2021) to solve the maximum image separation angle of the lensed quasar (when multiple images are produced).

## References

Ahumada, R., Allende Prieto, C., Almeida, A., et al. 2020, *ApJS*, 249, 3  
Allgood, B., Flores, R. A., Primack, J. R., et al. 2006, *MNRAS*, 367, 1781

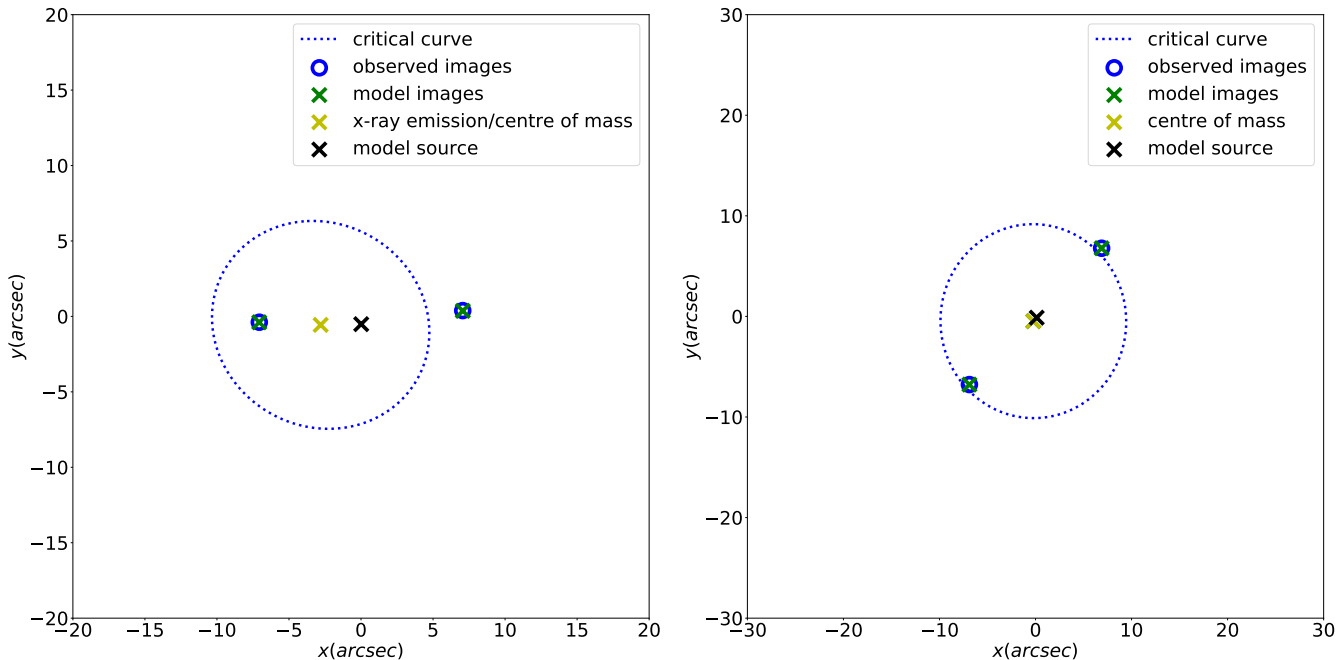


**Fig. A.3.** Left panel: Lens model for J110121.67+060931.3, the system shown in Figure A.1, assuming that the lens centre is fixed at the plausible X-ray emission peak. Right panel: Lens model solution J150155.61–025728.4, the system shown in Figure A.2, assuming that the lens centre is fixed at the galaxy north of the bright central star whose spectroscopic redshift is  $z = 0.89$ .

Andika, I. T., Suyu, S. H., Cañameras, R., et al. 2023, A&A, 678, A103  
 Anguita, T., Schmidt, R. W., Turner, E. L., et al. 2008, A&A, 480, 327  
 Bayliss, M. B., Sharon, K., Acharyya, A., et al. 2017, ApJ, 845, L14  
 Birrer, S. & Amara, A. 2018, Physics of the Dark Universe, 22, 189  
 Birrer, S., Shajib, A., Gilman, D., et al. 2021, The Journal of Open Source Software, 6, 3283  
 Blanton, M. R., Bershady, M. A., Abolfathi, B., et al. 2017, AJ, 154, 28  
 Böhringer, H., Schuecker, P., Guzzo, L., et al. 2004, A&A, 425, 367  
 Boylan-Kolchin, M., Ma, C.-P., & Quataert, E. 2008, MNRAS, 383, 93  
 Bulbul, E., Liu, A., Kluge, M., et al. 2024, The SRG/eROSITA All-Sky Survey: The first catalog of galaxy clusters and groups in the Western Galactic Hemisphere  
 Chambers, K. C., Magnier, E. A., Metcalfe, N., et al. 2016, arXiv e-prints, arXiv:1612.05560  
 Chan, J. H. H., Wong, K. C., Ding, X., et al. 2023, Survey of Gravitationally Lensed Objects in HSC Imaging (SuGOHI). IX. Discovery of Strongly Lensed Quasar Candidates  
 Child, H. L., Habib, S., Heitmann, K., et al. 2018, ApJ, 859, 55  
 Cloonan, A. P., Khullar, G., Napier, K. A., et al. 2024, COOL-LAMPS VIII: Known wide-separation lensed quasars and their host galaxies reveal a lack of evolution in  $M_{\text{BH}}/M_{\star}$  since  $z \sim 3$   
 Collaboration, D., Abareshi, B., Aguilar, J., et al. 2022, The Astronomical Journal, 164, 207  
 Collaboration, D., Abdul-Karim, M., Adame, A. G., et al. 2025, Data Release 1 of the Dark Energy Spectroscopic Instrument  
 Collaboration, D., Aghamousa, A., Aguilar, J., et al. 2016, The DESI Experiment Part I: Science, Targeting, and Survey Design  
 Cutri, R. M., Wright, E. L., Conrow, T., et al. 2013, Explanatory Supplement to the AllWISE Data Release Products, Explanatory Supplement to the AllWISE Data Release Products, by R. M. Cutri et al.  
 Dahle, H., Gladders, M. D., Sharon, K., et al. 2013, ApJ, 773, 146  
 Dawes, C., Storfer, C., Huang, X., et al. 2022, Finding Multiply-Lensed and Binary Quasars in the DESI Legacy Imaging Surveys, arXiv:2208.06356 [astro-ph]  
 Dawson, K. S., Kneib, J.-P., Percival, W. J., et al. 2016, The Astronomical Journal, 151, 44  
 Dawson, K. S., Schlegel, D. J., Ahn, C. P., et al. 2013, AJ, 145, 10  
 De Rosa, A., Vignali, C., Bogdanović, T., et al. 2019, New A Rev., 86, 101525  
 Dey, A., Schlegel, D. J., Lang, D., et al. 2019, AJ, 157, 168  
 Diemer, B. 2018, ApJS, 239, 35  
 Ding, J., Dalal, R., Strauss, M., et al. 2023, in American Astronomical Society Meeting Abstracts, Vol. 241, American Astronomical Society Meeting Abstracts, 460.24  
 Eisenstein, D. J., Weinberg, D. H., Agol, E., et al. 2011, AJ, 142, 72  
 Fian, C., Muñoz, J. A., Jiménez-Vicente, J., et al. 2024, A&A, 689, A129  
 Foreman-Mackey, D., Hogg, D. W., Lang, D., & Goodman, J. 2013, Publications of the Astronomical Society of the Pacific, 125, 306312  
 Fu, Y., Wu, X.-B., Li, Y., et al. 2024, ApJS, 271, 54  
 Gaia Collaboration, Bailer-Jones, C. A. L., Teyssier, D., et al. 2023a, A&A, 674, A41  
 Gaia Collaboration, Brown, A. G. A., Vallenari, A., et al. 2021, A&A, 649, A1  
 Gaia Collaboration, Vallenari, A., Brown, A. G. A., et al. 2023b, A&A, 674, A1  
 Golse, G. & Kneib, J. P. 2002, A&A, 390, 821  
 Gorski, K. M., Wandelt, B. D., Hansen, F. K., Hivon, E., & Banday, A. J. 1999, arXiv e-prints, astro  
 He, Z., Chen, Q., Deng, L., et al. 2025, A&A, 695, A76  
 He, Z., Li, N., Cao, X., et al. 2023, A&A, 672, A123  
 He, Z., Li, R., Shu, Y., et al. 2025, Using Convolutional Neural Networks to Search for Strongly Lensed Quasars in KiDS DR5  
 Hennawi, J. F., Myers, A. D., Shen, Y., et al. 2010, ApJ, 719, 1672  
 Hogg, D. W. 2000, Distance measures in cosmology  
 Hopkins, P. F., Bahcall, N. A., & Bode, P. 2005, ApJ, 618, 1  
 Hutsemékers, D., Sluse, D., Savić, D., & Richards, G. T. 2023, A&A, 672, A45  
 Inada, N., Oguri, M., Morokuma, T., et al. 2006, ApJ, 653, L97  
 Inada, N., Oguri, M., Pindor, B., et al. 2003, Nature, 426, 810  
 Jing, L., Chen, Q., Deng, Z., et al. 2025, A Quasar Pair Catalog Compiled from DESI DR1  
 Kochanek, C. S. 2020, MNRAS, 493, 1725  
 Lauer, T. R., Postman, M., Strauss, M. A., Graves, G. J., & Chisari, N. E. 2014, ApJ, 797, 82  
 Lemon, C., Anguita, T., Auger-Williams, M. W., et al. 2022, MNRAS  
 Levi, M., Bebek, C., Beers, T., et al. 2013, The DESI Experiment, a whitepaper for Snowmass  
 Lindegren, L., Hernández, J., Bombrun, A., et al. 2018, A&A, 616, A2  
 Lyke, B. W., Higley, A. N., McLane, J. N., et al. 2020, ApJS, 250, 8  
 Marocco, F., Eisenhardt, P. R. M., Fowler, J. W., et al. 2021, ApJS, 253, 8  
 Martin, G., Kaviraj, S., Devriendt, J. E. G., Dubois, Y., & Pichon, C. 2018, MNRAS, 480, 2266  
 Martinez, M. N., Napier, K. A., Cloonan, A. P., et al. 2023, The Astrophysical Journal, 946, 63  
 Merloni, A., Lamer, G., Liu, T., et al. 2024, A&A, 682, A34  
 Misawa, T., Inada, N., Oguri, M., et al. 2014, ApJ, 794, L20  
 Misawa, T., Inada, N., Ohsuga, K., et al. 2013, AJ, 145, 48  
 Misawa, T., Saez, C., Charlton, J. C., et al. 2016, The Astrophysical Journal, 825, 25  
 Motta, V., Mediavilla, E., Falco, E., & Muñoz, J. A. 2012, ApJ, 755, 82  
 Napier, K., Gladders, M., Sharon, K., et al. 2023, COOL-LAMPS. V. Discovery of COOL J0335–1927, a Gravitationally Lensed Quasar at  $z=3.27$  with an Image Separation of 23.3"

Navarro, J. F., Frenk, C. S., & White, S. D. M. 1997, *The Astrophysical Journal*, 490, 493508

Oguri, M., Ofek, E. O., Inada, N., et al. 2008, *The Astrophysical Journal*, 676, L1L4

Oguri, M., Rusu, C. E., & Falco, E. E. 2014, *MNRAS*, 439, 2494

Pâris, I., Petitjean, P., Aubourg, É., et al. 2018, *A&A*, 613, A51

Planck Collaboration, Aghanim, N., Akrami, Y., et al. 2020, *A&A*, 641, A6

Plionis, M., Barrow, J. D., & Frenk, C. S. 1991, *MNRAS*, 249, 662

Reiprich, T. H. & Böhringer, H. 2002, *ApJ*, 567, 716

Richards, G. T., Fan, X., Newberg, H. J., et al. 2002, *AJ*, 123, 2945

Robertson, A., Smith, G. P., Massey, R., et al. 2020, *MNRAS*, 495, 3727

Roedig, C., Krolik, J. H., & Miller, M. C. 2014, *ApJ*, 785, 115

Romero, G. E., Vila, G. S., & Pérez, D. 2016, *A&A*, 588, A125

Sehgal, N., Addison, G., Battaglia, N., et al. 2013, *ApJ*, 767, 38

Sharon, K., Bayliss, M. B., Dahle, H., et al. 2020, *ApJS*, 247, 12

Sharon, K., Bayliss, M. B., Dahle, H., et al. 2017, *ApJ*, 835, 5

Shen, Y., Hall, P. B., Horne, K., et al. 2019, *ApJS*, 241, 34

Shu, Y., Koposov, S. E., Evans, N. W., et al. 2019, *Monthly Notices of the Royal Astronomical Society*, 489, 47414759

Shu, Y., Marques-Chaves, R., Evans, N. W., & Pérez-Fournon, I. 2018, *Monthly Notices of the Royal Astronomical Society: Letters*, 481, L136L140

Sluse, D., Hutssemékers, D., Courbin, F., Meylan, G., & Wambsganss, J. 2012, *A&A*, 544, A62

Sonnenfeld, A. 2021, *A&A*, 656, A153

Stern, D., Djorgovski, S. G., Krone-Martins, A., et al. 2021, *ApJ*, 921, 42

Suto, D., Kitayama, T., Nishimichi, T., Sasaki, S., & Suto, Y. 2016, *Publications of the Astronomical Society of Japan*, 68

Suyu, S. H., Treu, T., Hilbert, S., et al. 2014, *ApJ*, 788, L35

Walsh, D., Carswell, R. F., & Weymann, R. J. 1979, *Nature*, 279, 381

Wen, Z. L. & Han, J. L. 2024, A catalog of 1.58 million clusters of galaxies identified from the DESI Legacy Imaging Surveys

Wong, K. C., Suyu, S. H., Chen, G. C. F., et al. 2020, *MNRAS*, 498, 1420

York, D. G., Adelman, J., Anderson, Jr., J. E., et al. 2000, *AJ*, 120, 1579

Zhang, Y., Jeltema, T., Hollowood, D. L., et al. 2019, *MNRAS*, 487, 2578

Zou, H., Gao, J., Xu, X., et al. 2021, *The Astrophysical Journal Supplement Series*, 253, 56

Zou, H., Zhou, X., Fan, X., et al. 2017, *PASP*, 129, 064101